IEEE Access
Multidisciplinary | Rapid Review | Open Access Journal

Received March 16, 2021, accepted March 24, 2021, date of publication March 26, 2021, date of current version April 5, 2021.

Digital Object Identifier 10.1109/ACCESS.2021.3069118

Novel Converter Topology With Reduced Cost, Size and Weight for High-Power Medium-Voltage Machine Drives: 3x3 Modular Multilevel Series Converter

GUSTAVO F. GONTIJO[1], (Member, IEEE), SONGDA WANG[2], (Student Member, IEEE), TAMAS KEREKES[1], (Senior Member, IEEE), AND REMUS TEODORESCU[1], (Fellow, IEEE)

[1]Department of Energy Technology, Aalborg University, 9220 Aalborg East, Denmark
[2]Department of Electrical Engineering, Eindhoven University of Technology, 5612 AZ Eindhoven, The Netherlands

Corresponding author: Songda Wang (s.wang6@tue.nl)

ABSTRACT The modular multilevel converter is considered the state-of-the-art power electronic solution for high-power high-voltage applications that require a DC stage and that operate with fixed frequency at their AC terminals. However, in high-power AC-AC variable-frequency applications, it has been proved that this converter topology presents an unnecessarily large number of components and an intolerably high submodule-capacitor voltage ripple at low frequencies. The modular multilevel matrix converter was proposed as a promising alternative for high-power medium-voltage electrical-machine drives since it presented improved performance at low frequencies and a reduced number of components in comparison to the modular multilevel converter resulting in reduced costs and improved efficiency. Even though, the modular multilevel matrix converter is one of the converter solutions that stands out the most for high-power machine drives, it presents some operational drawbacks such the unstable behavior under unbalanced grid conditions and the extremely complex internal control and modulation. Recently, a new converter topology named modular multilevel series converter was proposed presenting attractive operational characteristics such as the high performance at low frequencies, high performance under unbalanced grid conditions, and straightforward control and modulation, which are important advantages compared to the modular multilevel converter and the modular multilevel matrix converter. Nonetheless, as demonstrated in this paper, the modular multilevel series converter presents large component count and poor efficiency. Thus, in this paper, a new converter solution is proposed, which is an enhanced version of the modular multilevel series converter that preserves the previously mentioned advantageous operational characteristics and that presents an improved efficiency and a considerably reduced number of components in comparison to the other three converter topologies, resulting in reduced cost, size and weight.

INDEX TERMS High-power machine drives, high-power converters.

I. INTRODUCTION

With the development of the modern industry, many different high-power electrical-machine-drive applications are emerging such as the large wind turbines, flexible pumped-hydro-storage systems and heavy industrial drives. Upscaling is a trend in the wind power industry, which aims to obtain turbines with higher power ratings in order to optimize the total cost, size and weight of the wind power plant [1]–[3].

The associate editor coordinating the review of this manuscript and approving it for publication was Shaopeng Wu.

Flexible hydro turbines in the pumped-hydro-storage configuration are high-power energy storage systems that can provide many ancillary services to assist in the preservation of the power system stability, contributing to the high penetration of renewable-energy generation [4]–[6]. With the constantly increasing power ratings of these applications, at a certain point a medium-voltage structure (machine, converter, etc.) results in more efficient solutions with reduced currents. Moreover, the reduced currents allow for the usage of smaller conductors, which leads to solutions with considerably reduced cost, size and weight. Proper power

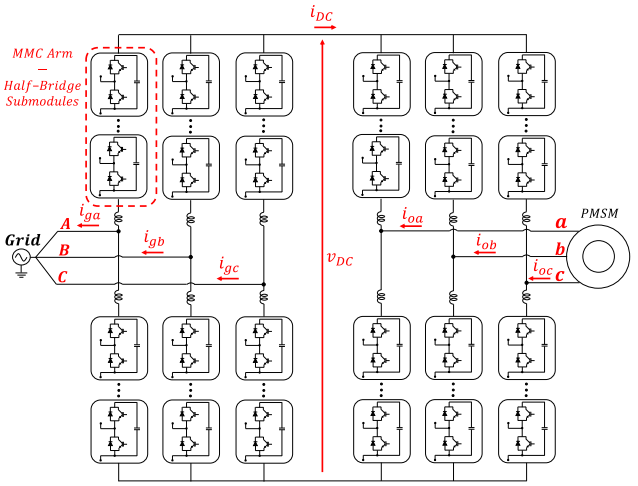

FIGURE 1. MMC topology.

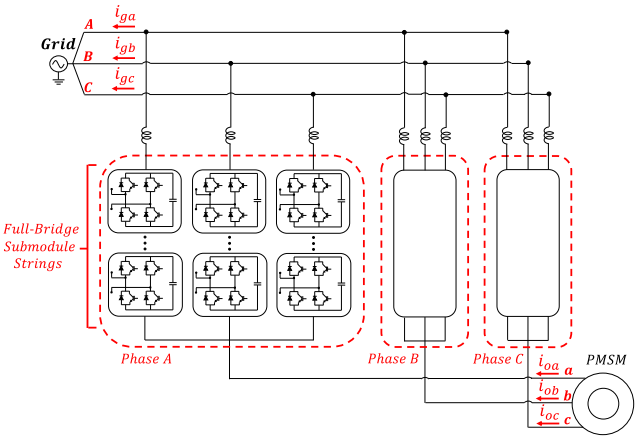

FIGURE 2. M^{3}C topology.

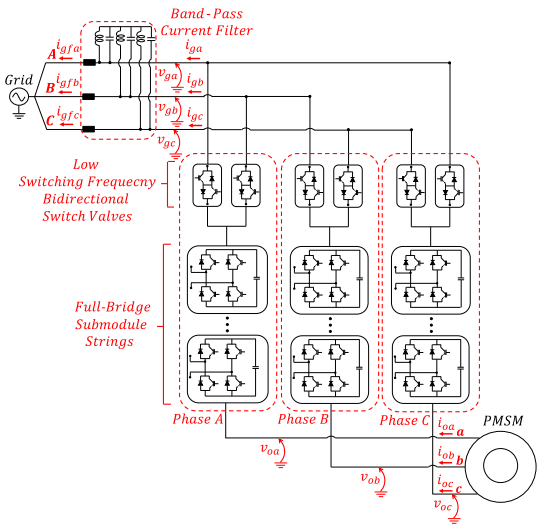

FIGURE 3. MMSC topology.

electronic converters are required to drive the mentioned systems as they must be capable to handle such high-power and medium-voltage levels while operating with a wide frequency range, including extremely low frequency values as, for example, in the case of the pumped-hydro-storage systems that must cross the 0-Hz operation point when switching from generation mode to pump mode and vice versa.

The modular multilevel converter (MMC), illustrated in Fig. 1, is the standard solution for high-power high-voltage applications that operate with fixed frequency at their AC terminals such as the high-voltage-direct-current (HVDC) transmission systems. The MMC can reach high voltages using the low-voltage semiconductor devices that are currently available in the industry and it operates with high power quality, high reliability and low switching frequency due to its modular multilevel structure. However, the MMC presents poor performance at variable-frequency operation since an intolerably high and dangerous submodule-capacitor voltage ripple occurs at low frequencies [7]–[11]. This high voltage ripple can exceed the voltage ratings of the semiconductor devices leading to their destruction. Furthermore, the MMC presents problems dealing with unbalanced grid conditions [12], [13] and many internal control loops are required for its proper operation. Nonetheless, one of the most critical drawbacks of the MMC is its large number of components, which leads to high costs, size and weight, as well as high conduction losses. Thus, the investigation of alternative converter topologies for high-power medium-voltage machine drives is a topic with high research interest nowadays.

The modular multilevel matrix converter (M^{3}C) [3], [14], also known as modular multilevel cascade converter based on triple-star bridge-cells (MMCC-TSBC) [15], [16], is one of the solutions that stands out the most for high-power machine drives since it presents improved performance at low frequencies and a reduced number of components, in comparison to the MMC, leading to reduced costs, size, weight, and reduced conduction losses. The M^{3}C (shown in Fig. 2), however, presents an unstable behavior under unbalanced grid conditions [17], [18] and extremely complex internal control and modulation are required for its proper operation, which are highly unattractive features.

Recently, a new converter topology named modular multilevel series converter (MMSC) was proposed [19] as a promising solution for high-power machine-drive applications and its topology is depicted in Fig. 3. The MMSC presents many operational advantages in relation to the MMC such as the reduced submodule-capacitor voltage ripple at low frequencies and the improved performance under unbalanced grid conditions [19]. Moreover, undesired circulating currents are nonexistent in the MMSC operation and the bulky and heavy arm/string inductors are not required for the proper operation of the MMSC. These are consequences of the decoupled and independent nature of the MMSC phases. The MMSC presents a straightforward control, with few internal control loops, which is an advantageous characteristic in relation to the MMC. As explained in [19], the MMSC also presents important operational advantages in comparison to the M^{3}C such as the stable performance under unbalanced grid conditions, and the much more straightforward

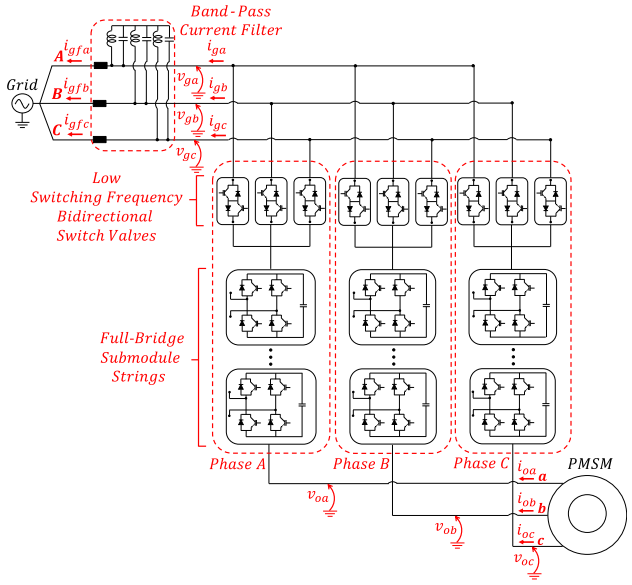

FIGURE 4. 3x3-MMSC topology.

control and modulation. Despite these advantages, the MMSC presents a higher number of components and worse efficiency in comparison to the M^{3}C, as will be demonstrated later in this paper.

To overcome the MMSC constructive drawbacks, a new converter solution is proposed in this paper, which is an improved version of the MMSC, and it is named 3×3 modular multilevel series converter (3x3-MMSC). The 3x3-MMSC topology is illustrated in Fig. 4 as it is a solution that preserves the operational advantages of the MMSC, in comparison to the MMC and the M^{3}C, and it presents improved structural characteristics. In this paper, a detailed comparative analysis among the MMC, the M^{3}C, the MMSC and the 3×3-MMSC is carried out, which is based on number of components and conduction losses. This analysis proves that the new 3x3-MMSC presents a considerably reduced number of semiconductor devices and of submodule capacitors in comparison to the M^{3}C, resulting in reduced cost, size and weight. Moreover, the 3x3-MMSC presents equivalent efficiency in relation to the M^{3}C. In this paper, simulation results are presented to demonstrate the 3x3-MMSC behavior while driving a permanent magnet synchronous machine (PMSM), in both generator and motor modes, representing a real machine-drive application. Moreover, a mathematical description of the 3x3-MMSC submodule-capacitor voltage ripple is proposed, which can be used to design the converter capacitors. Finally, experimental results are presented to validate the 3x3-MMSC performance under variable-frequency operation.

II. IMPROVED CONVERTER TOPOLOGY

As presented in detail in [19], the MMSC is composed of strings of full-bridge (FB) submodules and of bidirectional-switch valves connecting each string to two different phases of the grid. Since this converter is supposed to be used in medium-voltage applications, then the bidirectional-switch valves might need to be built with series-connected semiconductor devices in order to be able to withstand the grid voltage. However, since these are medium-voltage levels and not high-voltage ones, only few semiconductor devices connected in series are required, especially considering the availability of modern semiconductor devices with voltage ratings of up to 10 kV [20]. There are some products currently available in the industry that are valves composed of several series-connected semiconductor devices and that operate with high reliability due to advanced drivers that ensure static and dynamic voltage sharing among the series-connected devices [21]. These valves could be used to build the MMSC bidirectional-switch valves. Moreover, an important characteristic of the MMSC bidirectional-switch valves is that they operate with an extremely low switching frequency (equal to 50 or 60 Hz, which is the grid frequency). With the low switching frequency, it is easier to guarantee safe dynamic voltage sharing among the series-connected devices and low switching losses are obtained.

In this paper, the 3x3-MMSC is presented as a converter topology similar to the MMSC but with the addition of a third bidirectional-switch valve connecting each submodule string to the third phase of the grid. In other words, instead of having two bidirectional-switch valves, connecting each submodule string to two different phases of the grid, the 3x3-MMSC is composed of nine bidirectional-switch valves in total, or three bidirectional-switch valves connecting each submodule-string to each of the three phases of the grid (3 × 3). At first glance, it might seem that the 3x3-MMSC would be a converter solution with an increased number of components in comparison to the MMSC. However, it is quite the opposite. The addition of the third bidirectional-switch valve, to each submodule string, allows for the reduction of the voltage at the input terminals of the converter, still being possible to synthesize the same voltage amplitude at the load terminals. This fact allows for the reduction of the number of series-connected semiconductor devices that compose the bidirectional-switch valves, which both improves the converter reliability and reduces the total number of semiconductor devices composing the converter solution. Moreover, the number of components composing the submodule strings is also reduced. In fact, as will be shown in detail in this paper, the 3x3-MMSC is a converter solution with a considerably reduced number of semiconductor devices and with an extremely reduced number of the bulky and heavy submodule capacitors in comparison to the MMC, the M^{3}C and the MMSC. Besides, the 3x3-MMSC preserves the operational advantages in relation to the MMC and the M^{3}C such as the the low submodule-capacitor voltage ripple at low frequencies, the improved performance under unbalanced grid conditions and the straightforward control and modulation. Thus, the 3x3-MMSC should be a promising industrial solution for high-power medium-voltage machine drives.

As described in detail in [19], the MMSC operates synthesizing a given series voltage across the submodule string (v_s), depending on the instantaneous value of the grid voltage (v_g), in order to obtain the desired voltage at the load terminals according to a given reference ($v_o = v_{ref}$). Thus, through Kirchhoff's law, for the phase-A case the following equation is obtained:

$$v_{sa} = v_{refa} - v_{ga} \tag{1}$$

The operation described in (1) corresponds to the situation in which the bidirectional-switch valve that connects the phase-A string to phase A of the grid is in on state and the bidirectional-switch valve that connects the phase-A string to phase B of the grid is in off state. As explained in detail in [19], the average value of the voltage in each submodule capacitor of a given string converges to approximately $\frac{V_g}{N}$, in steady state, according to Kirchhoff's law and conservation of energy. V_g is the phase-to-ground, peak value of the grid voltage. Neglecting the submodule-capacitor voltage ripple, it means that if all the submodules of a given string are simultaneously inserted, the voltage synthesized in series by the MMSC is equal to V_g, which is the maximum voltage that the converter can synthesize. At some moments, the instantaneous value of the voltage to be synthesized in series is higher than V_g ($|v_{sa}| > V_g$) and, then, the MMSC would lose control over the load voltage. At these moments, the bidirectional-switch valves are used to connect the phase-A submodule string to phase B of the grid and, thus, the new value of the voltage to be synthesized in series is equal to the one described in equation (2), which is necessarily lower than V_g ($|v_{sa}| < V_g$) and, this way, the MMSC maintains control over the load voltage.

$$v_{sa} = v_{refa} - v_{gb} \tag{2}$$

As an illustrative example, in Fig. 5(a), one can observe the MMSC phase-A load-voltage reference (v_{refa}), which is a signal with amplitude equal to $V_o = 10$ kV, and frequency equal to $f_o = 10$ Hz in this case. The MMSC is connected to a grid with voltage amplitude equal to $V_g = 20$ kV and frequency equal to $f_i = 50$ Hz. The phase-A and phase-B of the grid voltage (v_{ga} and v_{gb}, respectively) are also depicted in Fig. 5(a). This figure illustrates one of the most important design criteria of the MMSC. In other words, the moment highlighted in Fig. 5(a) illustrates a situation in which the peak of the voltage reference meets the moment in which v_{ga} and v_{gb} have the same instantaneous value (equal to $-\frac{V_g}{2}$) and opposite polarity in relation to the reference. This is the worst-case scenario that corresponds to the highest value of v_{sa}, no matter if the submodule string is connected to phase A or phase B of the grid. In this example, this moment corresponds to an instant in which the instantaneous value of the voltage reference is equal to $v_{refa} = V_o = 10$ kV, and the instantaneous value of phase A and phase B of the grid voltage is equal to $v_{ga} = v_{gb} = -\frac{V_g}{2} = -\frac{20}{2} = -10$ kV. Thus, at this moment, the voltage that must be synthesized in series is equal to $|v_{sa}| = |V_o - (-\frac{V_g}{2})| = 20$ kV, no matter if the submodule string is connected to phase A or phase B of the grid. Fortunately, this is equal to the maximum voltage that the MMSC can synthesize ($V_{smax} = V_g = 20$ kV). For example, if the grid-voltage amplitude were equal $V_g = 18$ kV instead, then, at the same moment illustrated in Figure 5(a), the voltage to be synthesized in series would be equal to $|v_{sa}| = |V_o - (-\frac{V_g}{2})| = 10 + 9 = 19$ kV but the maximum voltage that the MMSC would be able to synthesize would be equal to $V_{smax} = V_g = 18$ kV. Thus, the MMSC would lose control over the load voltage. To sum up, this analysis defines the minimum grid voltage value so that the MMSC can always synthesize the desired load voltage. In other words:

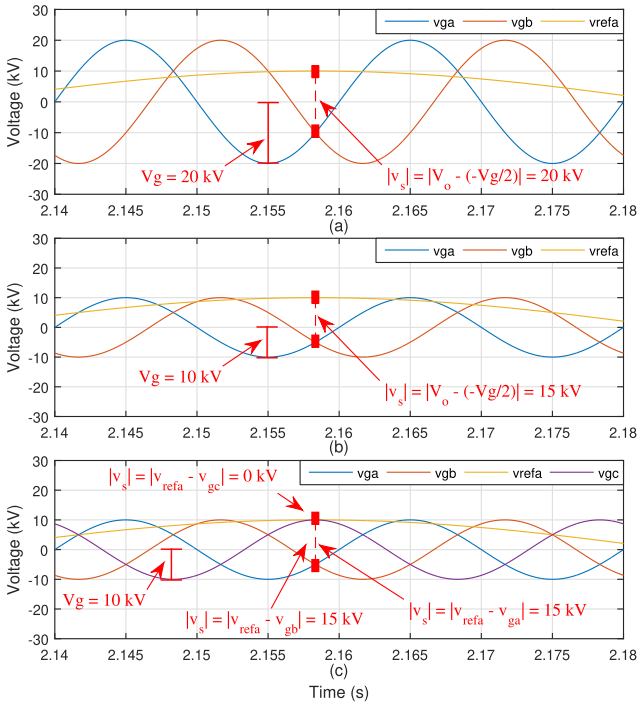

FIGURE 5. Explanation of the design criteria of the MMSC and the 3x3-MMSC. (a), (b) and (c) show the phase-A voltage reference (v_{refa}), along with the grid-voltage phases (v_{ga}, v_{gb} and also v_{gc} in (c)).

$$V_{smax} = V_g \geq V_o + \frac{V_g}{2} \tag{3}$$

And thus:

$$V_g \geq 2V_o \tag{4}$$

Let us now analyze the situation illustrated in Figure 5(b). In this case, the MMSC phase-A load-voltage reference (v_{refa}) is still a signal with amplitude equal to $V_o = 10$ kV, and frequency equal to $f_o = 10$ Hz. The grid voltages, however, are signals with amplitude equal to $V_g = 10$ kV and frequency equal to $f_i = 50$ Hz. The phase-A and phase-B of the grid voltage (v_{ga} and v_{gb}, respectively) are also depicted in Figure 5(b). It is obvious that the moment highlighted in Figure 5(b) corresponds to a situation in which the MMSC would lose control over the load voltage since the voltage

that would have to be synthesized in series (v_{sa}) would be higher than $V_g = 10$ kV, which is the maximum voltage that the converter can synthesize. In other words, $|v_{sa}| = |V_o - (-\frac{V_g}{2})| = 10 + 5 = 15$ kV, no matter if the submodule string were connected to phase A or phase B of the grid, which is higher than $V_g = 10$ kV.

Let us now analyze the situation illustrated in Figure 5(c), which represents the 3x3-MMSC operation since the third phase of the grid voltage (v_{gc}) is added. The addition of the voltage v_{gc} illustrates the addition of the third bidirectional-switch valve that can be used to connect the phase-A submodule string to phase C of the grid. The instant highlighted in Figure 5(c) is exactly the same as the one illustrated in Figure 5(b) in which $|v_{sa}| = 15$ kV, no matter if the submodule string is connected to phase A or phase B of the grid, and $V_g = 10$ kV. It is very important to notice that if the submodule string is connected to phase C of the grid, however, the value of the voltage to be synthesized by the converter becomes $|v_{sa}| = |v_{refa} - v_{gc}| = 10 - 10 = 0$ kV, which is obviously lower than $V_g = 10$ kV and, thus, it is possible to maintain control over the load voltage. The information illustrated in Figure 5(c) defines an important design criteria of the new 3x3-MMSC, which states that:

$$V_g \geq V_o \tag{5}$$

In theory, by analyzing Figure 5(c), it is possible to say that the amplitude of the voltage at the input terminals of the 3x3-MMSC (V_g) could even be lower than the amplitude of the load-voltage reference (V_o) and still maintain control over the load voltage for all operation points. However, in reality this is unfeasible as the 3x3-MMSC is not capable of operating in the boost mode. So, the theoretical limit for designing the 3x3-MMSC is the one described in equation (5).

III. INTERNAL CONTROL AND MODULATION

In Fig. 6 the internal control and modulation of the 3x3-MMSC phase A are explained. It is very important to emphasize that since this is a three-phase converter composed of three completely independent and decoupled single-phase structures, then no circulating currents exist in its operation. Thus, there is no need of a circulating-current-suppression control as in the MMC and M^{3}C case. Moreover, due to the three decoupled submodule strings, no constraints exist in order for the 3x3-MMSC to operate in a safe and reliable fashion, which is an advantage over the M^{3}C that presents constraints of not creating short-circuit paths among its nine submodule strings. In fact, the 3x3-MMSC presents a straightforward internal control which is based only on the switching logic of the bidirectional-switch valves and on the voltage balance among the submodule capacitors of each string. As described in Fig. 6, the first step of the control is to calculate the error ($E = v_{refa} - v_{ga}$), which is equal to the voltage that must be synthesized across the submodule string (v_{sa}), according to equation (1), in order to obtain the desired voltage at the load terminals

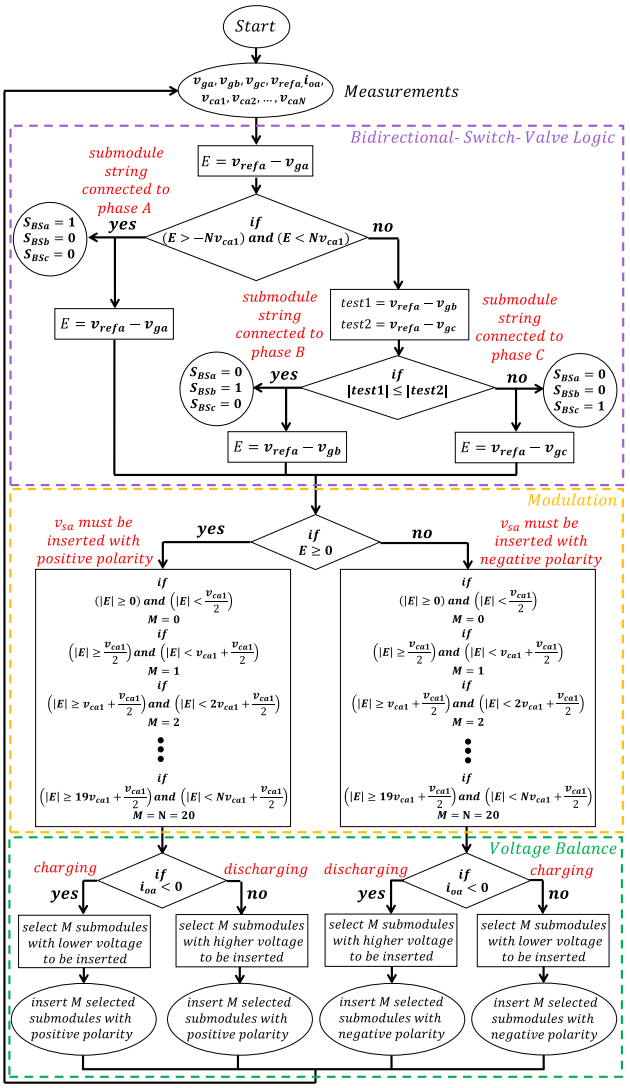

FIGURE 6. Flowchart of 3x3-MMSC internal control and modulation.

($v_{oa} = v_{refa}$). After that, it is necessary to check if the instantaneous value calculated of E is within the limits of $-Nv_{ca1}$ and Nv_{ca1}. In other words, considering that the voltage-balancing control is working, the 3x3-MMSC presents N submodules available to be inserted. Each of these submodules presents a capacitor voltage equal to $v_{ca1} = v_{ca2} = \ldots = v_{caN}$. Thus, if the value of E is within the mentioned limits, it means that the submodule string is capable of synthesizing in series the necessary voltage to obtain the desired load voltage. In this case, the phase-A submodule string is kept connected to phase A of the grid as the bidirectional-switch valve that connects the phase-A string to phase A of the grid is kept in on state ($S_{BSa} = 1$) and the bidirectional-switch valves that connect the phase-A string to phases B and C of the grid are kept in off state ($S_{BSb} = 0$ and $S_{BSc} = 0$, respectively). Moreover, E is still calculated as $E = v_{refa} - v_{ga}$.

If E is not within the mentioned limits, however, then the phase-A submodule string must be connected to phase B

or C of the grid. In order to decide to which one of them, two test variables are calculated: $test1 = v_{refa} - v_{gb}$ and $test2 = v_{refa} - v_{gc}$. The absolute values of $test1$ and $test2$ are compared and if the absolute value of $test1$ is smaller or equal to the absolute value of $test2$, then the submodule string should be connected to phase B of the grid, which means that $S_{BSa} = 0$, $S_{BSb} = 1$, $S_{BSc} = 0$ and $E = v_{refa} - v_{gb}$. If the absolute value of $test1$ is bigger than the absolute value of $test2$, then the submodule string should be connected to phase C of the grid, which means that $S_{BSa} = 0$, $S_{BSb} = 0$, $S_{BSc} = 1$ and $E = v_{refa} - v_{gc}$. The next step is the modulation that decides the polarity of the submodules to be inserted, as well as the number of submodules to be inserted (M) according to the instantaneous value calculated of E, which is equal to the voltage that must be synthesized in series, across the submodule string, in order to obtain the desired voltage at the load terminals ($v_{oa} = v_{refa}$). Finally, after the modulation, the submodule-capacitor voltage-balancing control is carried out, which depending on the polarity of the submodules to be inserted and on the direction of the load current (i_{oa}), decides which M submodules of the N submodules available should be inserted. If at the given moment i_{oa} is a charging current, then the M submodules with lower capacitor voltages are selected to be inserted and if i_{oa} is a discharging current, then the M submodules with higher capacitor voltages are selected to be inserted. This way, it is possible to maintain all the submodules in a given string with balanced voltage values.

IV. COMPARATIVE ANALYSIS

The comparative analysis carried out in this section is based on the number of components and conduction losses of the converter topologies. As described in detail in [19], the conduction losses are much more influential than the switching losses in the total semiconductor-device losses of the converter topologies with modular multilevel structure in medium-voltage levels, which explains why the efficiency analysis is only based on conduction losses. The fair component-count comparative analysis requires that the IGBTs used to design all the converter topologies have the exact same collector-to-emitter voltage (V_{CES}). Nonetheless, as will be explained in detail in this section, the converter topologies require IGBTs with different current ratings. Thus, the authors adopted as references two commercial IGBTs from the same series of SEMIKRON. The first is the SEMITRANS 2 SKM 145GB176D that presents the following characteristics: collector-to-emitter voltage equal to $V_{CES} = 1.7$ kV, nominal collector current equal to $i_{Cnom} = 100$ A and unit price equal to US$ 61.55. The second IGBT is the SEMITRANS 2 SKM 100GB176D that presents the following characteristics: collector-to-emitter voltage equal to $V_{CES} = 1.7$ kV, nominal collector current equal to $i_{Cnom} = 75$ A and unit price equal to US$ 52.47. It is important to emphasize that, even though these IGBTs have different current ratings, their collector-to-emitter saturation voltage, their unit weight and unit volume are the same. In other words, both IGBTs present collector-to-emitter saturation voltage equal to $V_{CE(sat)} = 2$ V, unit weight equal to 0.16 kg and unit volume equal to 95.88 cm^3. The IGBT prices are based on online catalogues, which is enough for the comparison sake. However, these prices could vary for real industrial applications depending on their production volume. In order to facilitate the component-count calculations, a simplification is made, which consists in considering $V_{CES} = 1.5$ kV. Another simplification is made, which consists in considering the forward voltage of the IGBT anti-parallel diode to be equal to the IGBT collector-to-emitter saturation voltage and, thus, the same conduction loss is obtained no matter the direction of the current flowing through the IGBTs. Finally, to obtain a fair comparative analysis, it is considered that all the converters must synthesize a load voltage equal to $V_o = 10$ kV (phase-to-ground peak value), while supplying power to the same RL load, resulting in an identical AC current with rms value equal to $I_{AC} = 100$ A.

A. MMC

1) NUMBER OF COMPONENTS

The MMC DC-link voltage should be designed according to [19]:

$$V_{DC} \geq 2V_o \tag{6}$$

In other words, the DC-link voltage should ideally be equal to $V_{DC} = 2V_o$, which is the minimum voltage possible that makes the MMC capable to synthesize the desired voltage V_o. Nonetheless, in order to account for the submodule-capacitor voltage ripple and to avoid overmodulation issues, the MMC DC-link voltage will be designed according to $V_{DC} = 1.25(2V_o)$, which corresponds to a 25% voltage margin. This exact same margin will be adopted in the design of all the converter topologies so that a fair comparison is obtained. The MMC DC-link voltage is, then, designed with a value equal to $V_{DC} = 1.25(2V_o) = 25$ kV since $V_o = 10$ kV. Moreover, the sum of the DC values of the capacitor voltages of each submodule in one arm should be equal to V_{DC}, which means that the submodule-capacitor voltage should be equal to $\frac{V_{DC}}{N}$, in which N is the number of submodules composing the MMC arm. For safety reasons, the IGBT collector-to-emitter voltage is typically designed with two times the value of the nominal capacitor voltage ($V_{CES} = 2(\frac{V_{DC}}{N})$). Thus, the number of submodules in each MMC arm should be calculated as follows:

$$N = 2(\frac{V_{DC}}{V_{CES}}) \tag{7}$$

Since $V_{CES} = 1.5$ kV, then the number of submodules in each arm must be equal to $N = 33.33 \approx 34$ submodules. Considering that this is a back-to-back MMC, then the entire solution presents twelve arms with half-bridge (HB) submodules. Each HB submodule is composed of two IGBTs and of one capacitor. This way, the MMC solution is composed of $12 \times 34 \times 2 = 816$ IGBTs and of $12 \times 34 \times 1 = 408$ capacitors.

2) CONDUCTION LOSSES

The current that flows through each MMC arm, considering that all the undesired AC-circulating-current components are suppressed, is equal to:

$$I_{arm} = \frac{I_{AC}}{2} + \frac{I_{DC}}{3} \tag{8}$$

In which I_{DC} is the DC-link current. In order to obtain a relationship between the AC and DC currents, it is considered that the converter AC-side power is equal to the DC-side one ($P_{AC} = P_{DC}$) and that the reactive power is null. In other words:

$$\sqrt{3}(\frac{\sqrt{3}}{\sqrt{2}})V_o I_{AC} = V_{DC} I_{DC} \tag{9}$$

Equation (9) can be rewritten as follows:

$$I_{DC} = (\frac{3}{\sqrt{2}})\frac{V_o}{V_{DC}} I_{AC} \tag{10}$$

By substituting $V_o = 10$ kV and $V_{DC} = 25$ kV into (10), the following is obtained:

$$I_{DC} = 0.85 I_{AC} \tag{11}$$

By substituting (11) into (8), the following is obtained:

$$I_{arm} = 0.78 I_{AC} \tag{12}$$

This is a back-to-back MMC and it is considered that the same AC voltage that is synthesized at the load side ($V_o = 10$ kV) is also synthesized at the grid side, and it is considered that the grid-side power profile is equal to the load-side power profile in such a way that the AC current injected into the grid presents the same rms value as the load current (equal to I_{AC}). Thus, the arm current, described in (12), flows simultaneously through the twelve arms of the MMC. Since the MMC is composed of HB submodules, then the arm current flows through one IGBT per submodule, no matter if the submodule is inserted or by-passed. This way, the arm current flows simultaneously through $12 \times 34 \times 1 = 408$ IGBTs. The MMC conduction losses can be calculated as follows:

$$P_{CLoss} = 408 V_{CE(sat)} I_{arm} \tag{13}$$

By substituting equation (12), $V_{CE(sat)} = 2$ V and $I_{AC} = 100$ A into equation (13), the MMC conduction losses are obtained, which are equal to:

$$P_{CLoss} = 63.65 \text{ kW} \tag{14}$$

B. M^{3}C

1) NUMBER OF COMPONENTS

As explained in Fig. 7, the maximum line-to-line voltage that the M^{3}C can synthesize is equal to:

$$V_{oLL} = 2 V_{string} \tag{15}$$

In which V_{string} corresponds to the maximum voltage possible to be synthesized by one string if all its submodules are simultaneously inserted. Since $V_{oLL} = \sqrt{3} V_o$, then the string voltage required to obtain the desired load voltage (V_o) is ideally calculated as follows:

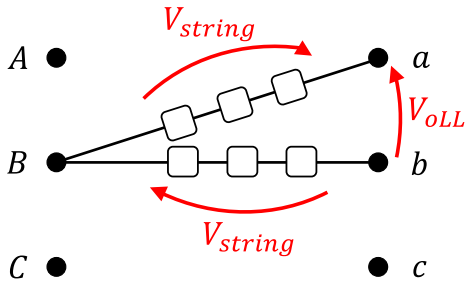

FIGURE 7. M^{3}C voltage representation.

$$V_{string} \geq \frac{\sqrt{3} V_o}{2} \tag{16}$$

Similarly to the MMC case, in order to account for the submodule-capacitor voltage ripple and to avoid overmodulation issues, the M^{3}C string voltage is designed according to $V_{string} = 1.25(\frac{\sqrt{3}V_o}{2})$. Since $V_o = 10$ kV, then $V_{string} = 10.83$ kV. The M^{3}C capacitor voltage should be equal to $\frac{V_{string}}{N}$, in which N is the number of submodules composing the M^{3}C string. Once again, the IGBT collector-to-emitter voltage is typically designed with two times the value of the nominal capacitor voltage ($V_{CES} = 2(\frac{V_{string}}{N})$). Thus, the number of submodules composing each M^{3}C string can be calculated as follows:

$$N = 2(\frac{V_{string}}{V_{CES}}) \tag{17}$$

Since $V_{CES} = 1.5$ kV, then $N = 14.44 \approx 15$ submodules per string. The M^{3}C is composed of nine strings of FB submodules. Each FB submodule is composed of four IGBTs and of one capacitor. This way, the M^{3}C solution is composed of $9 \times 15 \times 4 = 540$ IGBTs and of $9 \times 15 \times 1 = 135$ capacitors.

2) CONDUCTION LOSSES

The current that flows through each M^{3}C string, considering that all the undesired AC-circulating-current components are suppressed, is equal to:

$$I_{string} = \frac{I_g}{3} + \frac{I_o}{3} \tag{18}$$

In which I_g and I_o are the rms values of the grid and load currents, respectively. As previously defined, $I_o = I_{AC}$. The same assumption as in the MMC case is adopted, which consists in considering that the M^{3}C synthesizes the voltage V_o at both load and grid terminals, and that the grid-side power profile is equal to the load-side power profile in such a way that $I_g = I_o = I_{AC}$. Equation (18) can be rewritten as:

$$I_{string} = \frac{I_{AC}}{3} + \frac{I_{AC}}{3} = 0.667 I_{AC} \tag{19}$$

The string current, represented in equation (19), flows simultaneously through the nine strings of the M^{3}C. Since the

M^3C is composed of FB submodules, then the string current flows through two IGBTs per submodule, no matter if the submodule is inserted or by-passed. Thus, the string current flows simultaneously through $9 \times 15 \times 2 = 270$ IGBTs. Finally, the M^3C conduction losses can be calculated as follows:

$$P_{CLoss} = 270 V_{CE(sat)} I_{string} \tag{20}$$

By substituting (19), $V_{CE(sat)} = 2$ V and $I_{AC} = 100$ A into (20), the M^3C conduction losses are obtained, which are equal to:

$$P_{CLoss} = 36.02 \text{ kW} \tag{21}$$

C. MMSC

1) NUMBER OF COMPONENTS

The amplitude of the grid voltage, connected to the input terminals of the MMSC, should be designed according to equation (4), which means that, ideally, $V_g = 2V_o$. However, similarly to the other topologies, a voltage margin is considered and, thus, $V_g = 1.25(2V_o)$ is adopted for the MMSC design. Since $V_o = 10$ kV, then $V_g = 25$ kV. The average value of the voltage in each submodule capacitor is equal to $\frac{V_g}{N}$. Once again, the IGBT collector-to-emitter voltage is typically designed with a value two times higher than the nominal capacitor voltage ($V_{CES} = 2(\frac{V_g}{N})$). Thus, the number of submodules composing each MMSC submodule string can be calculated as follows:

$$N = 2(\frac{V_g}{V_{CES}}) \tag{22}$$

Since $V_{CES} = 1.5$ kV, then the number of submodules is equal to $N = 33.33 \approx 34$ submodules per string. The entire three-phase solution is composed of three strings of FB submodules. Each FB submodule is composed of four IGBTs and of one capacitor. This way, the MMSC submodule strings are composed of $3 \times 34 \times 4 = 408$ IGBTs and of $3 \times 34 \times 1 = 102$ capacitors. However, the components of the bidirectional-switch valves must also be considered. These valves must withstand the peak value of the line-to-line grid voltage, which is equal to $\sqrt{3}V_g = 43.3$ kV. Each bidirectional-switch cell is composed of two IGBTs connected in series. The two IGBTs can be triggered simultaneously (using a dead-time technique in combination with a snubber circuit) because of the low switching frequency of the bidirectional-switch valves that allows to avoid complex multi-step commutation techniques commonly applied to matrix converters [19]. This way, each bidirectional-switch cell can be regarded as a single semiconductor device with double the voltage ratings ($2V_{CES} = 3$ kV). Considering the same safety margin for the IGBT design, then the number of cells composing each bidirectional-switch valve should be calculated as follows:

$$N = 2(\frac{\sqrt{3}V_g}{2V_{CES}}) \tag{23}$$

Which results in $N = 28.87 \approx 29$ bidirectional-switch cells per bidirectional-switch valve. Each bidirectional-switch cell is composed of two IGBTs. The entire MMSC solution is composed of six bidirectional-switch valves. Thus, the total number of components composing the MMSC bidirectional-switch valves is equal to $6 \times 29 \times 2 = 348$ IGBTs. Finally, the entire MMSC solution is composed of $408 + 348 = 756$ IGBTs and of 102 capacitors.

2) CONDUCTION LOSSES

The current that flows through each MMSC submodule string is equal to:

$$I_{string} = I_{AC} \tag{24}$$

The current described in equation (24) flows simultaneously through the three submodule strings that compose the MMSC. Since the MMSC is composed of FB submodules, then the string current flows through two IGBTs per submodule, no matter if these submodules are inserted or by-passed. As previously defined, the MMSC is composed of thirty four FB submodules per string, thus, the string current flows simultaneously through $3 \times 34 \times 2 = 204$ IGBTs, only considering the submodule strings. However, the string current also flows through the bidirectional-switch valves. The two bidirectional-switch valves, that connect each submodule string to two different phases of the grid, operate in a complementary fashion. Thus, the string current flows, in total, through three bidirectional-switch valves (one for each phase) simultaneously. As previously defined, each bidirectional-switch valve is composed of twenty nine bidirectional-switch cells. Since these cells are composed of two series-connected IGBTs, thus the string current flows simultaneously through $3 \times 29 \times 2 = 174$ IGBTs. Considering both the submodule strings and the bidirectional-switch valves, the MMSC string current flows simultaneously through $204 + 174 = 378$ IGBTs. Then, the MMSC conduction losses can be calculated as follows:

$$P_{CLoss} = 378 V_{CE(sat)} I_{string} \tag{25}$$

By substituting equation (24), $V_{CE(sat)} = 2$ V and $I_{AC} = 100$ A into equation (25), the following is obtained:

$$P_{CLoss} = 75.6 \text{ kW} \tag{26}$$

D. 3x3-MMSC

1) NUMBER OF COMPONENTS

The amplitude of the grid voltage, connected to the input terminals of the 3x3-MMSC, should be designed according to equation (5), which means that, ideally, $V_g = V_o$. However, similarly to the other topologies, a voltage margin is considered and, thus, $V_g = 1.25(V_o)$ is adopted for the 3x3-MMSC design. Since $V_o = 10$ kV, then $V_g = 12.5$ kV. Similarly to the MMSC case, the number of submodules composing each string of the 3x3-MMSC should be calculated according to (22). Since $V_{CES} = 1.5$ kV, then the number of submodules must be equal to $N = 16.67 \approx 17$

submodules per string. The entire three-phase solution is composed of three strings of FB submodules. Each FB submodule is composed of four IGBTs and of one capacitor. This way, the 3x3-MMSC solution is composed of $3 \times 17 \times 4 = 204$ IGBTs and of $3 \times 17 \times 1 = 51$ capacitors. It is important to notice that since the voltage at the 3x3-MMSC input terminals is half of the voltage at the MMSC input terminals, then the 3x3-MMSC presents half the number of semiconductor devices and capacitors in relation to the MMSC, if only the submodule strings are considered. The 3x3-MMSC bidirectional-switch valves must be capable of blocking the voltage $\sqrt{3}V_g = 21.65$ kV. Once again, similarly to the MMSC case, the number of bidirectional-switch cells composing each bidirectional-switch valve of the 3x3-MMSC is calculated according to (23), which results in $N = 14.43 \approx 15$ bidirectional-switch cells per bidirectional-switch valve. Each bidirectional-switch cell is composed of two IGBTs. The entire 3x3-MMSC solution is composed of nine bidirectional-switch valves (see Fig. 4). Thus, the total number of components composing the 3x3-MMSC bidirectional-switch valves is equal to $9 \times 15 \times 2 = 270$ IGBTs. Finally, the entire 3x3-MMSC solution is composed of $204 + 270 = 474$ IGBTs and of 51 capacitors.

2) CONDUCTION LOSSES

The current described in equation (24) is the same that flows through the 3x3-MMSC strings as it flows, simultaneously, through the three submodule strings that compose the converter. Since the 3x3-MMSC is composed of FB submodules, then the string current flows through two IGBTs per submodule, no matter if these submodules are inserted or by-passed. The 3x3-MMSC is composed of seventeen FB submodules per string, thus, the string current flows simultaneously through $3 \times 17 \times 2 = 102$ IGBTs, only considering the submodule strings. However, the string current also flows through the bidirectional-switch valves. Only one of the three bidirectional-switch valves, that connect each submodule string to the three phases of the grid, conducts the string current at any time, while the other two are in off state. Thus, the string current flows, in total, through three bidirectional-switch valves (one for each phase) simultaneously. As previously defined, each bidirectional-switch valve is composed of fifteen bidirectional-switch cells. Since these cells are composed of two series-connected IGBTs, thus the string current flows simultaneously through $3 \times 15 \times 2 = 90$ IGBTs. Considering both the submodule strings and the bidirectional-switch valves, the 3x3-MMSC string current flows simultaneously through $102 + 90 = 192$ IGBTs. Then, the 3x3-MMSC conduction losses can be calculated as follows:

$$P_{CLoss} = 192 V_{CE(sat)} I_{string} \tag{27}$$

By substituting equation (24), $V_{CE(sat)} = 2$ V and $I_{AC} = 100$ A into equation (27), the following is obtained:

$$P_{CLoss} = 38.4 \text{ kW} \tag{28}$$

TABLE 1. Number of Components.

Component	MMC	M^{3}C	MMSC	3x3-MMSC
IGBTs	816	540	756	474
Capacitors	408	135	102	51

TABLE 2. Conduction Losses (P_{CLoss}).

MMC	M^{3}C	MMSC	3x3-MMSC
63.65 kW	36.02 kW	75.6 kW	38.4 kW

E. SUMMARY

In TABLE 1 and TABLE 2, one can observe the summary of the comparative analysis carried out in this section.

According to TABLE 1, the MMC in the back-to-back configuration presents the highest number of components with, especially, a considerably higher number of capacitors in comparison to all the other topologies. One important characteristic of the MMSC and the 3x3-MMSC is the reduced number of the bulky and heavy submodule capacitors. The MMSC presents a reduced number of capacitors in relation to the M^{3}C but it presents a higher number of semiconductor devices. The most important conclusion is that the 3x3-MMSC, proposed in this paper, is the solution with lower number of semiconductor devices and capacitors. The 3x3-MMSC presents a 12.22% reduction in the number of semiconductor devices and a 62.22% reduction in the number of capacitors in comparison to the M^{3}C. Nonetheless, according to (12), the MMC arm current is equal to $i_{arm} = 0.78 I_{AC} = 0.78 \times 100 = 78$ A, according to (19), the M^{3}C string current is equal to $i_{string} = 0.667 I_{AC} = 0.667 \times 100 = 66.7$ A, and according to (24), the MMSC and the 3x3-MMSC string currents are equal to $i_{string} = I_{AC} = 100$ A. This means that the MMC and the M^{3}C can be designed with the IGBTs with nominal current equal to $i_{Cnom} = 75$ A and unit price equal to US$ 52.47 while the MMSC and the 3x3-MMSC should be designed with the IGBTs with nominal current equal to $i_{Cnom} = 100$ A and unit price equal to US$ 61.55. Once again, both these IGBTs present unit weight equal to 0.16 kg and unit volume equal to 95.88 cm^3. Thus, with the number of components described in TABLE 1, and with the IGBTs unit price, unit weight and unit volume, previously described, the total semiconductor-device cost, weight and volume of each converter topology can be obtained as summarized in TABLE 3. By only considering the semiconductor devices, it is possible to conclude that the M^{3}C and the new 3x3-MMSC are the most competitive solutions as they present considerably reduced cost, weight and volume in comparison to the MMC and the MMSC (see TABLE 3). The 3x3-MMSC is slightly more expensive than the M^{3}C, even though they present quite similar costs. It is important to highlight that the new 3x3-MMSC is lighter and more compact than the M^{3}C.

Obviously, the submodule capacitors should also be analyzed to obtain the total cost, weight and volume of the converter topologies. These capacitors can be quite heavy

TABLE 3. Total Semiconductor-Device Cost, Weight and Volume.

Parameter	MMC	M^3C	MMSC	3x3-MMSC
N^o of IGBTs	816	540	756	474
Unit Price (US$)	52.47	52.47	61.55	61.55
Total Cost (US$)	42815	28333	46531	29174
Unit Weight (kg)	0.16	0.16	0.16	0.16
Total Weight (kg)	130.56	86.4	120.96	75.84
Unit Volume (cm^3)	95.88	95.88	95.88	95.88
Total Volume (cm^3)	78238	51775	72485	45447

and bulky as they can have a high influence in the total cost, weight and volume of the converters. The extremely reduced number of capacitors in comparison to the other topologies (see TABLE 1) is a quite strong indicative that the 3x3-MMSC would present a significantly reduced total cost, total weight and total volume in comparison to the other converter topologies if the submodule capacitors were taken into account. Since variable-frequency applications are considered (machine drives), then the size of the capacitors of each converter topology varies depending on the application since the submodule-capacitor voltage ripple is a function of the frequency at the AC terminals of the converters. In other words, the size of the capacitors should be evaluated for each specific application, taking into account the frequency range of operation of the given application. In order to demonstrate the behavior of the 3x3-MMSC submodule-capacitor voltage ripple (ΔV) in relation to the MMC submodule-capacitor voltage ripple, simulations were carried out in the software PSCAD/EMTDC. In these simulations, the MMC and the 3x3-MMSC were modeled with the same parameters described in this section, i.e., the MMC was modeled with $V_{DC} = 25$ kV and the 3×3 MMSC was modeled with $V_g = 12.5$ kV. Both converter topologies were built with identical submodule capacitors with capacitance value equal to 5 mF. Moreover, both converters were connected to a $f_i = 60$-Hz grid and both of them synthesized a $V_o = 10$-kV load voltage while supplying power to a RL load (100 Ω and 10 mH) resulting in an identical AC current flowing through the converters. In these simulations, the frequency of the voltage synthesized by the converters at the load terminals (f_o) varied, one by one Hz, until the whole frequency range was covered. The simulation results are shown in Fig. 8.

Many important conclusions can be obtained from Fig. 8. As expected [7]–[11], the MMC presented intolerably high submodule-capacitor voltage ripple at low frequencies, especially close to the 0-Hz operation point. The 3x3-MMSC, on the other hand, presented low submodule-capacitor voltage ripple at low frequencies and higher submodule-capacitor voltage ripple at high frequencies. In fact, as explained in detail in [19], [22], the MMSC submodule-capacitor voltage ripple increases as closer to the grid frequency (f_i) the load frequency (f_o) gets. This is the same behavior of the 3x3-MMSC submodule-capacitor voltage as illustrated in Fig. 8. The reason why the M^3C is not considered in Fig. 8

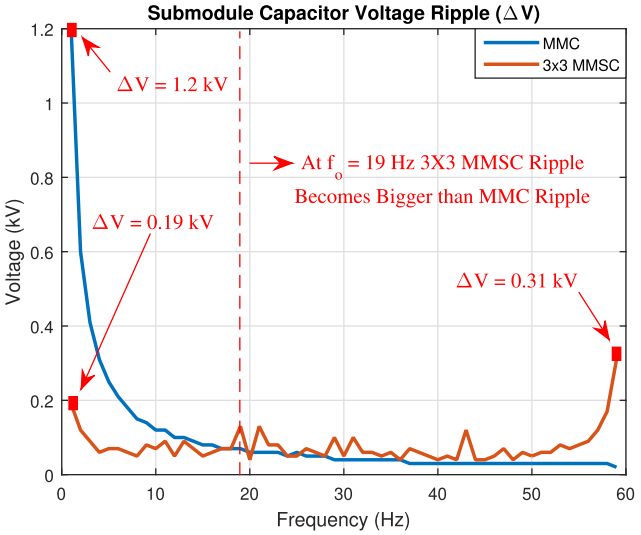

FIGURE 8. MMC and 3x3-MMSC submodule-capacitor voltage ripple for multiple frequency values.

is because this converter presents extremely complex control and modulation and its simulation is hard to reproduce and it is out of the scope of this paper. Moreover, the M^3C submodule-capacitor voltage ripple varies depending on the modulation adopted and, thus, a fair comparison would be hard to achieve. Nonetheless, it has been previously reported in the literature [23], [24] that the M^3C presents a reduced submodule-capacitor voltage ripple in comparison to the MMC at extremely low frequencies, but these two converter topologies present similar capacitor-voltage-ripple values for higher frequencies. The goal of Fig. 8 is to show that the 3x3-MMSC presents a reasonable submodule-capacitor voltage ripple for a wide frequency range of operation. In fact, the 3x3-MMSC presents a considerably smaller submodule-capacitor voltage ripple at low frequencies in comparison to the MMC. If these two converters were used to drive electrical machines in applications that operate close to the 0-Hz operation point (such as in pumped-hydro-storage systems or heavy industrial drives), then the 3x3-MMSC submodule capacitors could be considerably smaller than the MMC ones due to its high performance at low frequencies. As shown in Fig. 8, the 3x3-MMSC submodule-capacitor voltage ripple is smaller than the MMC one from $f_o = 0$ Hz until $f_o = 18$ Hz. The 3x3-MMSC submodule-capacitor voltage ripple only becomes higher than the MMC one at $f_o = 19$ Hz, and it remains only slightly higher than the MMC one until $f_o = 50$ Hz. So, for example, let us suppose that the 3x3-MMSC is used to drive a 50-Hz machine (operating between 0 Hz and 50 Hz) connected to a 60-Hz grid, then the 3x3-MMSC would always operate within a low-ripple region and its submodule capacitors could be small ones. Control techniques can be applied to the MMC to limit its submodule-capacitor voltage ripple at low frequencies, such as the modulation of an extra common-mode-voltage component in combination with the injection of circulating-current components [22]. However,

TABLE 4. Efficiency.

MMC	M^3C	MMSC	3x3-MMSC
97.00%	98.30%	96.43%	98.19%

these methods can lead to other problems. For example, huge overcurrents occur in the MMC arms due to the high peak values of the injected circulating-current components. Besides, the extra commom-mode voltage synthesized increases the voltage stress in the machine winding insulation and increases the shaft voltage, which could lead to bearing and shaft failures [22]. Even if the MMC low-frequency submoule-capacitor voltage-ripple is limited through control methods, the size of the 3x3-MMSC capacitors would still be quite similar to the size of the MMC capacitors as demonstrated in Fig. 8. Since the 3x3-MMSC presents a considerably reduced number of submodule capacitors in comparison to the MMC and the M^3C (see TABLE 1) and since the 3x3-MMSC capacitors do not need to be big ones (as explained in Fig. 8), then it is clear that the 3×3-MMSC should be a solution with considerably reduced cost, size and weight in comparison to the MMC and the M^3C.

Regarding the conduction-loss conclusions, since $V_o = 10$ kV and $I_{AC} = 100$ A, then the rated power of the four converter topologies is equal to:

$$P_{rated} = \sqrt{3}(\frac{\sqrt{3}}{\sqrt{2}}V_o)I_{AC} = 2.12MW \tag{29}$$

Using the conduction-loss values described in TABLE 2 and the rated power described in (29), the efficiency values of each topology were obtained (see TABLE 4). The MMC and the MMSC are the two most inefficient solutions with conduction-loss values considerably higher than the M^3C and the 3x3-MMSC. The M^3C and the 3×3-MMSC present quite similar efficiency values as described in TABLE 4.

V. MATHEMATICAL DESCRIPTION OF 3x3-MMSC SUBMODULE-CAPACITOR VOLTAGE RIPPLE

In this section, a detailed explanation of how to calculate the 3x3-MMSC submodule-capacitor voltage ripple is proposed. In order to carry out this analysis, let us consider phase A of the 3x3-MMSC. The voltage across the phase-A submodule string (v_{sa}) is controlled according to:

$$v_{sa} = v_{refa} - v_{ga} = V_o sin(\omega_o t) - V_g sin(\omega_i t) \tag{30}$$

In which $\omega_o = 2\pi f_o$, $\omega_i = 2\pi f_i$, f_o and f_i are the load and grid frequency, respectively, and V_o and V_g are the magnitude of the load and grid voltages, respectively. The 3x3-MMSC synthesizes a given series voltage (v_{sa}), depending on the instantaneous value of the grid voltage (v_{ga}), in order to obtain the voltage reference equal to v_{refa} at the load terminals. As previously mentioned, the average value of the voltages in each submodule capacitor naturally converges to approximately $\frac{V_g}{N}$ in steady state. Thus, if all the submodules are simultaneously inserted, then the voltage across the string is equal to V_g, which is the maximum voltage that the 3x3-MMSC can synthesize in series. Since $f_o \neq f_i$ is considered then, according to (30), there will be moments in which v_{sa} will be higher than V_g. At these moments, in order to keep control over the load voltage, the phase-A submodule string must be connected to either phase B or phase C of the grid. According to the 3x3-MMSC control diagram (see Fig. 6), if $|v_{refa} - v_{gb}|$ is smaller or equal to $|v_{refa} - v_{gc}|$, then the phase-A submodule string is connected to phase B of the grid and the voltage to be synthesized across the submodule string becomes equal to:

$$v_{sa} = v_{refa} - v_{gb} = V_o sin(\omega_o t) - V_g sin(\omega_i t - \frac{2\pi}{3}) \tag{31}$$

On the other hand, if $|v_{refa} - v_{gb}|$ is bigger than $|v_{refa} - v_{gc}|$, then the phase-A submodule string is connected to phase C of the grid and the voltage to be synthesized across the submodule string becomes equal to:

$$v_{sa} = v_{refa} - v_{gc} = V_o sin(\omega_o t) - V_g sin(\omega_i t + \frac{2\pi}{3}) \tag{32}$$

Clearly, the 3x3-MMSC string voltage is described by a discontinuous function that can be equal to (30), or equal to (31) or equal to (32), depending on the submodule-string connection with the grid. Thus, in order to analyze the 3x3-MMSC submodule-capacitor voltage ripple, a computer-based approach was required and a code implementation was adopted to describe the 3x3-MMSC string voltage. The code algorithm is illustrated in the flowchart of Fig. 9. Considering that the 3x3-MMSC supplies power to a RL load with values equal to R and L, then the phase-A load current can be calculated as follows:

$$i_{oa} = \frac{v_{refa}}{|R + j\omega_o L|} = \frac{V_o sin(\omega_o t + \theta)}{|R + j\omega_o L|} \tag{33}$$

In which θ is the load angle. The phase-A load current, described in (33), is the same current that flows through the 3x3-MMSC phase-A submodule string. Thus, the phase-A submodule-string power can be calculated as follows:

$$p_{sa} = v_{sa} i_{oa} \tag{34}$$

By integrating the string power the string energy is obtained as follows:

$$E_{sa} = \int p_{sa} dt \tag{35}$$

Finally, the 3x3-MMSC submodule-capacitor voltage ripple (Δv_{ca}) can be calculated as a function of the string energy (E_{sa}) according to the following equation as described in [25]:

$$E_{sa} = \frac{NC}{2}\Delta v_{ca}^2 \tag{36}$$

In order to validate the proposed model, the algorithm shown in Fig. 9 was implemented in a Matlab code with the following parameters: $V_g = 15$ kV, $V_o = 10$ kV, $f_i = 50$ Hz, $f_o = 1$, 10 and 45 Hz, $R = 100\ \Omega$, $L = 10$ mH, $N = 20$, $C = 5$ mF, $\Delta T = 0.0001$ and $T_{end} = 4$ s. Moreover,

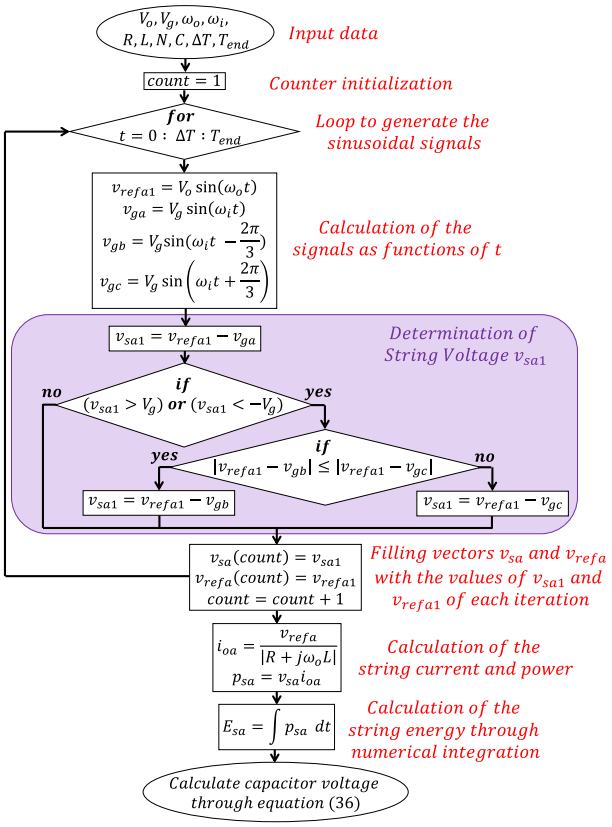

FIGURE 9. Flowchart of the algorithm implemented though a code to develop the analysis of the 3x3-MMSC submodule-capacitor voltage ripple.

the 3x3-MMSC topology (see Fig. 4) was implemented in the software PSCAD/EMTDC with equivalent parameters as the Matlab code and a simulation was carried out so that the simulation results could be compared with the results obtained through the model implemented in the Matlab code. The results obtained are depicted in Fig. 10 and Fig. 11. In Fig. 10(a), the string voltage signals (v_{sa}) obtained through both the Matlab code and the PSCAD/EMTDC simulation for the case in which $f_o = 10$ Hz are shown. In Fig. 10(b), a zoom of Fig. 10(a) is depicted. It is obvious the presence of the $f_o = 10$ Hz and the $f_i = 50$ Hz components in the v_{sa} signal, as expected. Moreover, it is important to observe the discontinuities in the v_{sa} signal that occurs every time v_{sa} reaches the limits equal to $\pm V_g = 15$ kV. At these moments, the phase-A sumbmodule string is connected to phase B or phase C of the grid. These discontinuities are the reason why a code-based approach is required to analyze the 3x3-MMSC submodule-capacitor voltage ripple. It is interesting to notice in Fig. 10(b), which is a zoom of Fig. 10(a), how the Matlab-code signal (named "Model Signal") matches the PSCAD signal with high accuracy. As expected, the PSCAD signal presents a staircase shape according to the multilevel-voltage characteristic of the converter. The model signal, on the other hand, is a continuous one.

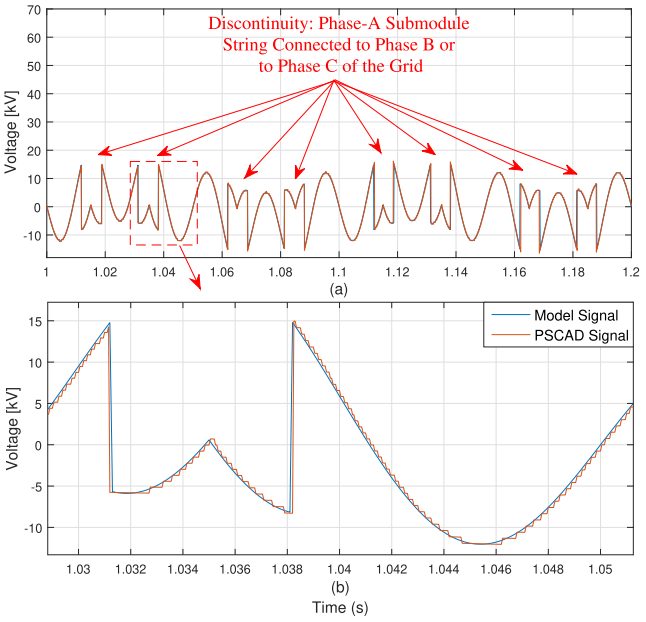

FIGURE 10. (a) String voltage signals (v_{sa}) obtained through Matlab code and PSCAD/EMTDC simulation for the case in which $f_o = 10$ Hz and (b) zoom of Fig. 10(a).

In Fig. 11(a), (c) and (e), one can observe the 3x3-MMSC submodule-capacitor voltage ripple (Δv_{ca}), obtained though the Matlab code, for the cases in which $f_o = 1, 10$ and 45 Hz, respectively. In Fig. 11(b), (d) and (f), one can observe the 3x3-MMSC submodule-capacitor voltage ripple (Δv_{ca}), obtained though the PSCAD simulation, for the cases in which $f_o = 1, 10$ and 45 Hz, respectively. It is important to notice that the waveform of the Matlab-code signals match the waveform of the PSCAD signals with high accuracy. Besides, the voltage-ripple amplitudes (ΔV) are also quite similar, which means that the proposed model is representing the real behavior of the 3x3-MMSC submodule-capacitor voltage with high precision. This model can be used to design the 3x3-MMSC submodule capacitors since it allows to estimate the capacitor voltage ripple as a function of the capacitance value. For example, one can provide a capacitance value as an input to the model of Fig. 9 and check the resulting submodule-capacitor voltage-ripple amplitude, in a trial and error fashion, until the desired ripple value is obtained.

VI. SIMULATION ANALYSIS

In this section, simulation results are presented, based on the software PSCAD/EMTDC, in which the 3x3-MMSC operates driving a PMSM through a field-oriented-control (FOC) technique as depicted in Fig. 12. In this control technique, the machine stator currents (i_{oabc}) are controlled in a rotating reference frame aligned with the rotor field (θ_R) in such a way that the direct-axis current component (i_{od}) is responsible for the machine reactive-power (Q_o) control and the in-quadrature-axis current component (i_{oq}) is responsible for the machine-speed (ω_R) control. The FOC algorithm

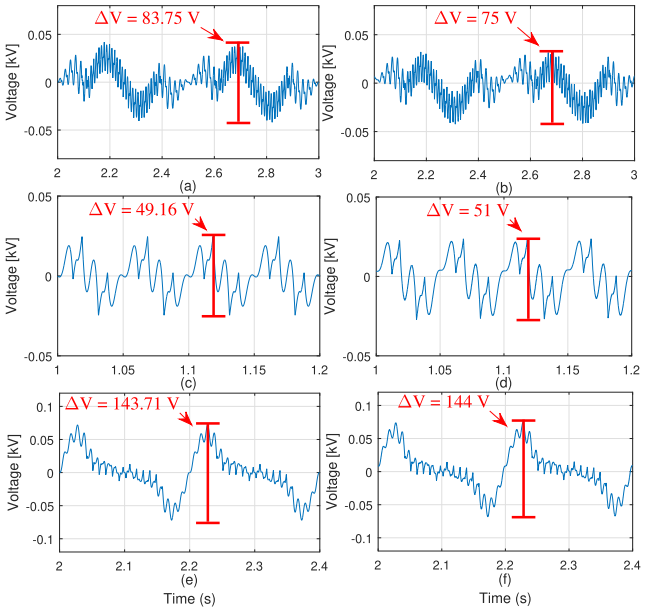

FIGURE 11. Submodule-capacitor voltage ripple (Δv_{ca}) obtained through Matlab code for the cases: (a) $f_o = 1$ Hz, (c) $f_o = 10$ Hz and (e) $f_o = 45$ Hz. Submodule-capacitor voltage ripple (Δv_{ca}) obtained through PSCAD simulation for the cases: (b) $f_o = 1$ Hz, (d) $f_o = 10$ Hz and (f) $f_o = 45$ Hz.

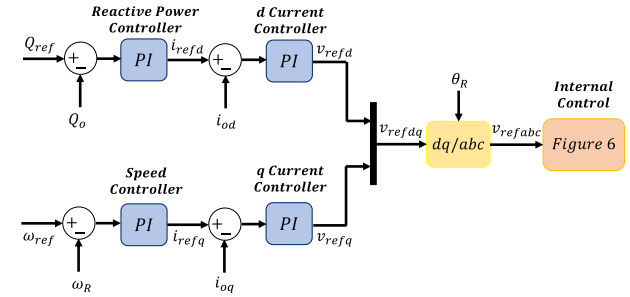

FIGURE 12. 3x3-MMSC closed-loop control based on FOC to drive PMSM.

generates the stator voltage references (v_{refabc}) that are provided to the 3x3-MMSC internal control and modulation illustrated in Fig. 6.

In this simulation, the 3x3-MMSC is composed of $N = 20$ FB submodules per string, of the nine bidirectional-switch valves and of the band-pass filter. The submodule-capacitor capacitance is equal to 5 mF and the band-pass filter presents the following parameters: $R = 25\ \Omega$, $L = 10.13$ mH and 1 mF. The converter is connected to a $V_g = 20$-kV grid (phase-to-ground, peak value) with frequency equal to $f_i = 50$ Hz. The PMSM rated power is equal to 3 MVA, its rated voltage is equal to 10 kV and its rated frequency is equal to 50 Hz. Initially, the PMSM speed reference is set to $\omega_{ref} = 0.2$ pu and the machine torque is set to 1 pu (generator mode). At $t = 3$ s, the speed reference changes to $\omega_{ref} = 0.4$ pu. At $t = 5$ s, the PMSM torque changes to 1.2 pu and, at $t = 7$ s, the PMSM torque changes to -1 pu (motor mode) as an active-power inversion occurs. The simulation results are illustrated in Fig. 13. In Fig. 13(a), one can observe the PMSM speed (ω_R) and it is clear that the 3x3-MMSC is

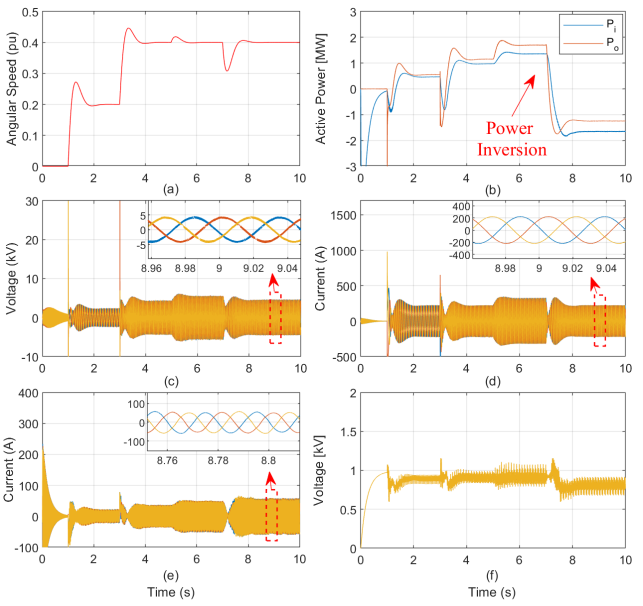

FIGURE 13. Active-power-inversion simulation results. (a) PMSM speed (ω_R), (b) 3x3-MMSC grid-side and load-side active power (P_i and P_o, respectively), (c) load voltage (v_{oabc}), (d) load current (i_{oabc}), (e) 50-Hz current injected into the grid (i_{gfabc}) and (f) phase-A submodule-string capacitor voltages (v_{ca1}, v_{ca2} $\cdots$ v_{ca20}).

capable to properly control the machine speed according to the reference provided. In Fig. 13(b), it is possible to analyze the 3x3-MMSC grid-side and load-side active power (P_i and P_o, respectively) that vary according to the machine-speed and machine-torque references previously mentioned. In this figure, one can notice the power inversion as the active power changes from a positive value (generator mode) to a negative value (motor mode). The power inversion aims to demonstrate that the 3x3-MMSC is capable to control an electrical machine operating in both motor mode and in generator mode. In Fig. 13(c) and (d), the load voltage (v_{oabc}) and current (i_{oabc}) are shown, respectively. From these signals, it is clear that the 3x3-MMSC is capable to synthesize a high-power-quality voltage even though this converter topology does not have arm inductors and no load-side filter was used. In Fig. 13(e), one can observe the currents injected into the grid by the 3x3-MMSC after the filtering stage (i_{gfabc}) and it is clear that these are also high-power-quality signals, basically only composed of a 50-Hz component, since the other current components are filtered out by the band-pass current filter. This statement can be confirmed by analyzing the power injected into the grid (P_i), which is illustrated in Fig. 13(b), which is a signal without pulsations. Finally, in Fig. 13(f), one can observe the phase-A-string submodule-capacitor voltages. It is important to emphasize that even the huge active-power variation at the load side (power inversion) only slightly affects the submodeule-capacitor voltages as they remain regulated and stable in steady state. Besides, the voltage ripple remains tolerable within the entire simulation period.

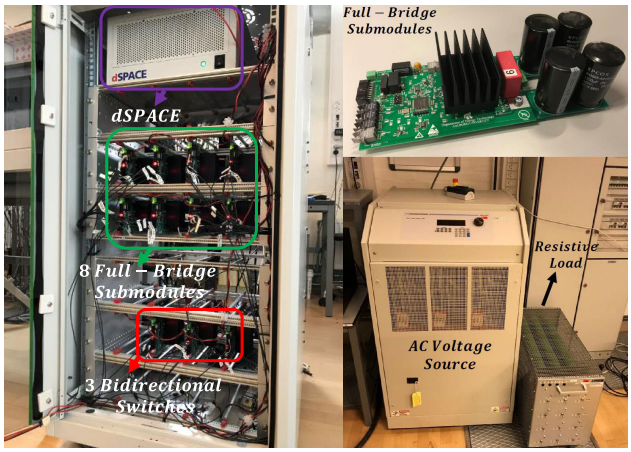

FIGURE 14. 3x3-MMSC test setup.

VII. EXPERIMENTAL VALIDATION

In this section, experimental results are presented to validate the 3x3-MMSC internal control and operational behavior for different frequency values. Since the 3x3-MMSC is a three-phase topology composed of three decoupled and independent single-phase converters, then a single-phase test setup is used to validate the mentioned characteristics of the converter. The experimental test setup is illustrated in Fig. 14 and it is composed of a string of eight FB submodules, of three bidirectional switches connecting the submodule string to each of the three phases of the grid, of an AC voltage source (AC power supply), representing the grid, and of a resistive load. All the semiconductor devices are IGBTs. In the experimental test, the 3x3-MMSC was connected to a grid with voltage equal to $V_g = 200$ V and frequency equal to $f_i = 50$ Hz. The load-voltage reference presented amplitude equal to $V_o = 150$ V and three different frequency values equal to $f_o = 1$, 10 and 45 Hz, while the 3x3-MMSC supplied power to a $100 - \Omega$ resistive load.

In Fig. 15(a), (c) and (e), the 3x3-MMSC submodule-capacitor voltages are shown for the cases $f_o = 1$, 10 and 45 Hz, respectively. In Fig. 15(b), (d) and (f), the load voltages synthesized by the 3x3-MMSC are shown, along with their references, for the cases $f_o = 1$, 10 and 45 Hz, respectively. In order to obtain a three-phase result, three different experimental tests were carried out (one for each phase), with the single-phase structure, resulting in the three-phase voltage waveform depicted in Fig. 15(b), (d) and (f).

As previously explained, the 3x3-MMSC presents low submodule-capacitor voltage ripple at low frequencies and its submodule-capacitor voltage ripple is deteriorated as the load frequency (f_o) comes close to the grid frequency ($f_i = 50$ Hz in this case). The experimental results shown in Fig. 15(a) prove that the 3x3-MMSC, indeed, presents low voltage ripple at low frequencies ($f_o = 1$ Hz). The 3x3-MMSC submodule-capacitor voltage ripple is increased for the 45-Hz case shown in Fig. 15(e). The zoom in the submodule-capacitor voltages illustrates that the sorting algorithm, responsible for the voltage-balance control, works

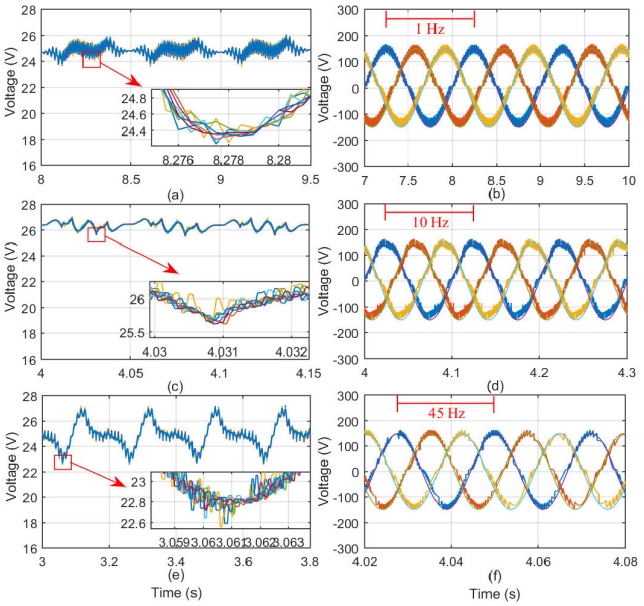

FIGURE 15. Experimental results. (a), (c) and (e) show the 3x3-MMSC submodule-capacitor voltages for the cases $f_o = 1$, 10 and 45 Hz, respectively. (b), (d) and (f) show the 3x3-MMSC load voltages (v_{oabc}) for the cases $f_o = 1$, 10 and 45 Hz, respectively.

properly since the capacitor voltages of all the submodules within the same string are kept balanced along time and with similar values. Finally, another conclusion is that the 3x3-MMSC is capable to synthesize the desired load voltage with different frequency values. In Fig. 15(b), (d) and (f), the actual switched voltages (without any filtering stage) synthesized at the load terminals are shown. These voltages are high-power-quality signals due to the multilevel characteristic of the 3x3-MMSC. In other words, the 8-levels 3x3-MMSC was capable to synthesize these high-power-quality voltages that would require only a small filter to filter out the high-order harmonics present in the signals.

In Fig. 16(a), the voltage across the submodule string (v_{sa}) is shown for the $f_o = 10$ Hz case. While the submodule string is kept connected to phase A of the grid, the voltage that should be synthesized across the submodule string, according to equation (1), is equal to the difference between the instantaneous value of the load-voltage reference (v_{refa}) and the instantaneous value of the phase-A grid voltage (v_{ga}). Thus, in Fig. 16(a), one can observe that the string voltage (v_{sa}) is, indeed, a signal composed of the $f_o = 10$-Hz and of the $f_i = 50$-Hz, during the period in which the submodule string is kept connected to phase A of the grid. The discontinuities in v_{sa} correspond to the moments in which this signal reaches the limits equal to approximately ± 200 V, which is the maximum voltage that the 3x3-MMSC can synthesize in series since the average voltage of the eight submodule capacitors is equal to approximately 25 V. In other words, at these moments, the submodule string must be connected to either phase B or phase C of the grid.

It is very important to notice that v_{sa} reaches the ± 200-V limits, in the worst-case scenario, every $\frac{1}{50\text{Hz}} = 20$ ms, which

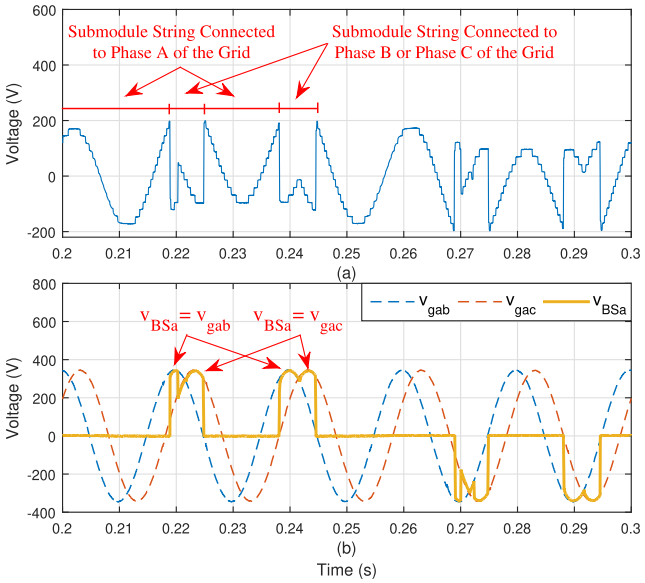

FIGURE 16. Experimental results. (a) Submodule-string voltage (v_{sa}) and (b) voltage across bidirectional-switch connecting submodule string and phase A of the grid (v_{BSa}) and two line-to-line grid voltages (v_{gab} and v_{gac}).

means that the bidirectional switches operate with a switching frequency of maximum 50-Hz. This experimental result proves an important feature of the 3x3-MMSC, i.e., its bidirectional switches operate with an extremely low switching frequency. In Fig. 16(b), one can observe the voltage across the bidirectional switch that connects the submodule string to phase A of the grid (v_{BSa}) along with the two line-to-line grid voltages v_{gab} and v_{gac}. Obviously, when the submodule string is connected to phase A of the grid, then $v_{BSa} = 0$ since the bidirectional switch is in conducting mode. When the submodule string is connected to phase B of the grid, then $v_{BSa} = v_{gab}$, and when the submodule string is connected to phase C of the grid, then $v_{BSa} = v_{gac}$.

VIII. CONCLUSION

In this paper, a new converter topology named 3x3-MMSC was proposed as a competitive solution for high-power medium-voltage machine drives due to its many operational and structural advantages in comparison to other alternative converter topologies. In this paper, a detailed comparative analysis among the 3x3-MMSC, the MMSC, the MMC and the M^{3}C was presented, proving that the proposed converter solution has a reduced number of semiconductor devices and an expressively reduced number of the bulky and heavy submodule capacitors in comparison to the MMC and the M^{3}C that are the converter topologies that stand out the most for high-power machine drives. Due to its considerably reduced number of components, the new 3x3-MMSC could be considered as a promising industrial solution for applications that require lightness and compactness. Besides, the 3x3-MMSC will be a solution with considerably reduced costs since the bulky submodule capacitors can be quite expensive. In this paper, simulation results were presented showing the low submodule-capacitor voltage ripple of the 3x3-MMSC at low frequencies, which is an important advantage in comparison to the MMC, especially for applications that operate close to the 0-Hz operation point such as pumped-hydro-storage systems and industrial motor drives. Moreover, simulation results were presented demonstrating that the 3x3-MMSC is capable to drive an electrical machine, in both generator and motor modes, while synthesizing high-power-quality voltages at the machine terminals and while injecting high-power-quality currents into the grid. Another contribution of this paper was the proposal of a mathematical model to describe the 3x3-MMSC submodule-capacitor voltage ripple, which can be used in the design stage of the converter capacitors. Finally, experimental results were presented to validate important characteristics of the 3x3-MMSC such as its behavior as a controlled voltage source from the load perspective, its high performance at low frequencies and the low-switching-frequency behavior of its bidirectional-switch valves.

REFERENCES

[1] M. Diaz, R. Cardenas, M. Espinoza, A. Mora, and P. Wheeler, "Modelling and control of the modular multilevel matrix converter and its application to wind energy conversion systems," in *Proc. 42nd Annu. Conf. IEEE Ind. Electron. Soc. (IECON)*, Oct. 2016, pp. 5052–5057.

[2] N. Fichaux *et al.*, "UPWIND—Design limits and solutions for very large wind turbines," Eur. Wind Energy Assoc., Brussels, Belgium, Tech. Rep., 2011. [Online]. Available: http://www.ewea.org/fileadmin/files/library/publications/reports/UpWind_Report.pdf

[3] M. Diaz, R. Cardenas, M. Espinoza, F. Rojas, A. Mora, J. C. Clare, and P. Wheeler, "Control of wind energy conversion systems based on the modular multilevel matrix converter," *IEEE Trans. Ind. Electron.*, vol. 64, no. 11, pp. 8799–8810, Nov. 2017.

[4] M. Basić, P. C. de Oliveira e Silva, and D. Dujić, "High power electronics innovation perspectives for pumped storage power plants," in *Proc. Hydro*, 2018, pp. 1–10. [Online]. Available: https://pel.epfl.ch

[5] M. Vasiladiotis, R. Baumann, C. Haderli, and J. Steinke, "IGCT-based direct AC/AC modular multilevel converters for pumped hydro storage plants," in *Proc. IEEE Energy Convers. Congr. Expo. (ECCE)*, Portland, OR, USA, Sep. 2018, pp. 4837–4844.

[6] P. K. Steimer, O. Senturk, S. Aubert, and S. Linder, "Converter-fed synchronous machine for pumped hydro storage plants," in *Proc. IEEE Energy Convers. Congr. Expo. (ECCE)*, Sep. 2014, pp. 4561–4567.

[7] M. Soares and E. H. Watanabe, "MMC applied to pumped hydro storage using a differentiable approximation of a square wave as common-mode voltage during low-frequency operation," in *Proc. IEEE 21st Workshop Control Modeling Power Electron. (COMPEL)*, Nov. 2020, pp. 1–8, doi: 10.1109/COMPEL49091.2020.9265759.

[8] A. J. Korn, M. Winkelnkemper, and P. Steimer, "Low output frequency operation of the modular multi-level converter," in *Proc. IEEE Energy Convers. Congr. Expo.*, Sep. 2010, pp. 3993–3997.

[9] M. Hagiwara, I. Hasegawa, and H. Akagi, "Start-up and low-speed operation of an electric motor driven by a modular multilevel cascade inverter," *IEEE Trans. Ind. Appl.*, vol. 49, no. 4, pp. 1556–1565, Jul. 2013.

[10] A. Antonopoulos, L. Angquist, S. Norrga, K. Ilves, L. Harnefors, and H.-P. Nee, "Modular multilevel converter AC motor drives with constant torque from zero to nominal speed," *IEEE Trans. Ind. Appl.*, vol. 50, no. 3, pp. 1982–1993, May 2014.

[11] Y. Okazaki, M. Hagiwara, and H. Akagi, "A speed-sensorless start-up method of an induction motor driven by a modular multilevel cascade inverter (MMCI-DSCC)," *IEEE Trans. Ind. Appl.*, vol. 50, no. 4, pp. 2671–2680, Jul. 2014.

[12] Z. Ou, G. Wang, and L. Zhang, "Modular multilevel converter control strategy based on arm current control under unbalanced grid condition," *IEEE Trans. Power Electron.*, vol. 33, no. 5, pp. 3826–3836, May 2018.

[13] C. Guo, J. Yang, and C. Zhao, "Investigation of small-signal dynamics of modular multilevel converter under unbalanced grid conditions," *IEEE Trans. Ind. Electron.*, vol. 66, no. 3, pp. 2269–2279, Mar. 2019.
[14] B. Fan, K. Wang, P. Wheeler, C. Gu, and Y. Li, "An optimal full frequency control strategy for the modular multilevel matrix converter based on predictive control," *IEEE Trans. Power Electron.*, vol. 33, no. 8, pp. 6608–6621, Aug. 2018.
[15] W. Kawamura, M. Hagiwara, and H. Akagi, "Control and experiment of a modular multilevel cascade converter based on triple-star bridge cells," *IEEE Trans. Ind. Appl.*, vol. 50, no. 5, pp. 3536–3548, Sep. 2014.
[16] W. Kawamura, K.-L. Chen, M. Hagiwara, and H. Akagi, "A low-speed, high-torque motor drive using a modular multilevel cascade converter based on triple-star bridge cells (MMCC-TSBC)," *IEEE Trans. Ind. Appl.*, vol. 51, no. 5, pp. 3965–3974, Oct. 2015.
[17] E. Behrouzian and M. Bongiorno, "Investigation of negative-sequence injection capability of cascaded H-bridge converters in star and delta configuration," *IEEE Trans. Power Electron.*, vol. 32, no. 2, pp. 1675–1683, Feb. 2017.
[18] S. Liu, M. Saeedifard, and X. Wang, "Analysis and control of the modular multilevel matrix converter under unbalanced grid conditions," *IEEE J. Emerg. Sel. Topics Power Electron.*, vol. 6, no. 4, pp. 1979–1989, Dec. 2018.
[19] G. Gontijo, S. Wang, T. Kerekes, and R. Teodorescu, "New AC–AC modular multilevel converter solution for medium-voltage machine-drive applications: Modular multilevel series converter," *Energies*, vol. 13, no. 14, p. 3664, Jul. 2020.
[20] V. Pala, E. V. Brunt, L. Cheng, M. O'Loughlin, J. Richmond, A. Burk, S. T. Allen, D. Grider, J. W. Palmour, and C. J. Scozzie, "10 kV and 15 kV silicon carbide power MOSFETs for next-generation energy conversion and transmission systems," in *Proc. IEEE Energy Convers. Congr. Expo. (ECCE)*, Sep. 2014, pp. 449–454.
[21] B. Jacobson, P. Karlsson, G. Asplund, L. Harnefors, and T. Jonsson, "VSC-HVDC transmission with cascaded two-level converters," in *Proc. CIGRE*, Paris, France, Aug. 2010, pp. B4–B110.
[22] G. Gontijo, S. Wang, T. Kerekes, and R. Teodorescu, "Performance analysis of modular multilevel converter and modular multilevel series converter under variable-frequency operation regarding submodule-capacitor voltage ripple," *Energies*, vol. 14, no. 3, p. 776, Feb. 2021.
[23] W. Kawamura and H. Akagi, "Control of the modular multilevel cascade converter based on triple-star bridge-cells (MMCC-TSBC) for motor drives," in *Proc. IEEE Energy Convers. Congr. Expo. (ECCE)*, Sep. 2012, pp. 3506–3513.
[24] A. J. Korn, M. Winkelnkemper, P. Steimer, and J. W. Kolar, "Direct modular multi-level converter for gearless low-speed drives," in *Proc. 14th Eur. Conf. Power Electron. Appl.*, Aug. 2011, pp. 1–7.
[25] L. Baruschka and A. Mertens, "A new three-phase AC/AC modular multilevel converter with six branches in hexagonal configuration," *IEEE Trans. Ind. Appl.*, vol. 49, no. 3, pp. 1400–1410, May 2013.

GUSTAVO F. GONTIJO (Member, IEEE) received the B.Sc. and M.Sc. degrees in electrical engineering from the Federal University of Rio de Janeiro (UFRJ), Rio de Janeiro, Brazil, in 2016 and 2018, respectively. He is currently pursuing the Ph.D. degree with the Department of Energy Technology, Aalborg University, Aalborg Øst, Denmark.

From 2014 to 2015, he was an Intern with the Leopoldo Americo Miguez de Mello Research and Development Center (Cenpes), Brazilian Energy Company Petrobras, where he was involved with research works about solar photovoltaic systems and wind turbines. From 2015 to 2019, he was with the Laboratory of Power Electronics and Medium Voltage Applications, which is part of the Alberto Luiz Coimbra Institute for Graduate Studies and Research in Engineering (COPPE/UFRJ). In 2020, he became a Research Assistant with the Department of Energy Technology, Aalborg University. His current research interests include ac–ac modular multilevel converter topologies applied to high-power medium-voltage machine drives, modern HVDC transmission systems, stability of power-electronic-based power systems, power-electronic solutions and control techniques applied to ac/dc microgrids, and power-electronic solutions to improve the power quality of wind turbines.

SONGDA WANG (Student Member, IEEE) was born in Harbin, China, in 1993. He received the Ph.D. degree in power electronics from Aalborg University, Denmark, in 2020. He currently holds a postdoctoral position with the Eindhoven University of Technology, The Netherlands. His current research interests include high voltage direct current (HVDC) system, modular multilevel converters (MMCs), and power-electronic-based power systems.

TAMAS KEREKES (Senior Member, IEEE) received the Diploma degree in electrical engineer from Technical University of Cluj, Romania, in 2002, with specialization in electric drives and robots, the Master of Science degree in power electronics and drives from the Department of Energy Technology Aalborg University, in 2005, and the Ph.D. degree in analysis and modeling of transformerless PV inverter systems from the Department of Energy Technology, Aalborg University, in 2009.

He is currently as an Associate Professor with Aalborg University. His research interests include grid connected renewable energy systems focusing on different grid forming and grid following control algorithms for power electronic converters for renewable energy systems with storage solutions.

REMUS TEODORESCU (Fellow, IEEE) received the Dipl.Ing. degree in electrical engineering from the Polytechnical University of Bucharest, Romania, in 1989, and the PhD. degree in power electronics from the University of Galati, Romania, in 1994.

In 1998, he joined the Department of Energy Technology, Aalborg University, power electronics section, where he currently works as a Full Professor. From 2013 to 2017, he was a Visiting Professor with Chalmers University of Technology, Sweden. He has coauthored the books *Grid Converters for Photovoltaic and Wind Power Systems* (Wiley-IEEE Press, 2011) and *Design, Control and Application of Modular Multilevel Converters for HVDC Transmission Systems* (Wiley-IEEE Press, 2016). He has coauthored over 500 IEEE journal and conference papers. His research interests include design and control of grid-connected converters for photovoltaic and wind power systems, HVDC/FACTS based on MMC, SiC-based converters, storage systems for utility based on Li-Ion battery technology, and battery lifetime model using artificial intelligence.